Biophysical Journal Volume 107 October 2014 1620–1628

Article

Traffic within the Cytochrome b_6f Lipoprotein Complex: Gating of the Quinone Portal

S. Saif Hasan,[1] Elizabeth A. Proctor,[2] Eiki Yamashita,[4] Nikolay V. Dokholyan,[3] and William A. Cramer[1,*]
[1]Department of Biological Sciences, Hockmeyer Hall of Structural Biology, Purdue University, West Lafayette, Indiana; [2]Curriculum in Bioinformatics and Computational Biology and [3]Department of Biochemistry and Biophysics, University of North Carolina, Chapel Hill, North Carolina; and [4]Osaka University, Institute for Protein Research, Suita, Osaka, Japan

ABSTRACT The cytochrome *bc* complexes b_6f and bc_1 catalyze proton-coupled quinol/quinone redox reactions to generate a transmembrane proton electrochemical gradient. Quinol oxidation on the electrochemically positive (p) interface of the complex occurs at the end of a narrow quinol/quinone entry/exit Q_p portal, 11 Å long in *bc* complexes. Superoxide, which has multiple signaling functions, is a by-product of the p-side quinol oxidation. Although the transmembrane core and the chemistry of quinone redox reactions are conserved in *bc* complexes, the rate of superoxide generation is an order of magnitude greater in the b_6f complex, implying that functionally significant differences in structure exist between the b_6f and bc_1 complexes on the p-side. A unique structure feature of the b_6f p-side quinol oxidation site is the presence of a single chlorophyll-*a* molecule whose function is unrelated to light harvesting. This study describes a cocrystal structure of the cytochrome b_6f complex with the quinol analog stigmatellin, which partitions in the Q_p portal of the bc_1 complex, but not effectively in b_6f. It is inferred that the Q_p portal is partially occluded in the b_6f complex relative to bc_1. Based on a discrete molecular-dynamics analysis, occlusion of the Q_p portal is attributed to the presence of the chlorophyll phytyl tail, which increases the quinone residence time within the Q_p portal and is inferred to be a cause of enhanced superoxide production. This study attributes a novel (to our knowledge), structure-linked function to the otherwise enigmatic chlorophyll-*a* in the b_6f complex, which may also be relevant to intracellular redox signaling.

INTRODUCTION

The integral membrane cytochrome *bc* lipoprotein complexes (cyt *bc* complexes) b_6f (Fig. 1, *A* and *B*) and bc_1 function at an intermediate redox position in the photosynthetic and respiratory electron transport chains, where they couple transmembrane proton translocation to electron transfer through redox reactions of lipophilic quinone/-ol, plastoquinone/-ol, and ubiquinone/-ol, respectively (1–6). Quinones (ubiquinone in respiratory membranes and plastoquinone (PQ) in photosynthetic membranes (Fig. 1 *C*)) contain a redox-active ring that is attached to a 45–50 carbon prenyl tail. On the electrochemically positive (p) side of *bc* complexes, quinol deprotonation-oxidation reactions within the p-side active (Q_p) site involve quinol entry into a portal 11 Å in depth (Q_p portal; Figs. 1 *B* and 2, *A–D*) that connects the Q_p site to the quinone pool in the lipid-filled intermonomer cavity of *bc* complexes, as described recently in detail for the b_6f complex (7). Due to the large size of the substrate quinol/quinone (Fig. 1, *C* and *D*), traffic through the Q_p portal suggests the possibility of a steric constraint in intraprotein quinone dynamics.

It has been shown that quinol/quinone redox reactions within the Q_p site of *bc* complexes serve as a significant source of superoxide production (Fig. 3) (8–16). Although the overall architecture and quinol redox chemistry in the p-side active site of cytochrome *bc* complexes are conserved (17), the rate of superoxide production is at least 10-fold higher in the b_6f complex (16). It has been proposed that p-side superoxide generation in *bc* complexes is a consequence of electron transfer to molecular oxygen from the anionic semiquinone formed through 1), quinol oxidation by the [2Fe-2S] cluster of the iron-sulfur subunit; and/or 2), electron transfer from the reduced heme b_p to the oxidized quinone (18). Despite the role of reactive oxygen species (ROS), including superoxide, in stress response, cellular signaling, and maintenance of homeostasis in photosynthetic organisms (19–22), the differences in crystal structure between the b_6f and bc_1 complexes relevant to superoxide generation have not been defined.

A feature that is unique to the structure of the cytochrome b_6f complex Q_p portal is the single chlorophyll-*a* (Chl) molecule in each monomer of the complex, which was first detected spectrophotometrically (23,24) and subsequently in crystal structures of the isolated dimeric b_6f complex (Fig. 1, *A* and *B*) obtained from the filamentous cyanobacteria *Mastigocladus laminosus* (PDB IDs 1VF5,

Submitted June 18, 2014, and accepted for publication August 5, 2014.
*Correspondence: waclab@purdue.edu
Editor: Lukas Tamm.

0006-3495/14/10/1620/9 $2.00
http://dx.doi.org/10.1016/j.bpj.2014.08.003

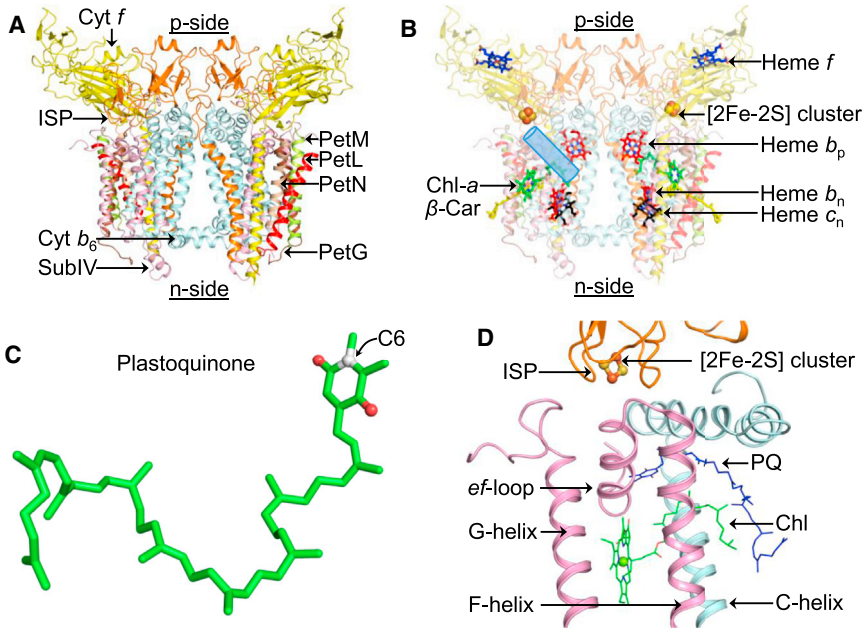

FIGURE 1 Dimeric cytochrome b_6f complex of oxygenic photosynthesis from *M. laminosus* (PDB ID 2E74). (*A*) Polypeptide composition of the b_6f complex. Color code showing the eight known subunits of the complex: cytochrome b_6, cyan; subunit IV, pink; cytochrome *f*, yellow; ISP, orange; PetL, red; PetM, green; PetG, brown; PetN, wheat. (*B*) Prosthetic groups in the cytochrome b_6f complex are shown as sticks. The Q_p portal is highlighted as a blue cylinder. (*C*) The PQ molecule, which serves as the substrate of cytochrome b_6f complex-catalyzed redox reactions. Carbon atoms are shown in green, with the exception of atom C6 (*white*). The oxygen atoms are shown in red. (*D*) Overview of the p-side quinone portal, showing both Chl (*green sticks*) and PQ (*blue sticks*).

2E74-76, 4H13, and 4H0L) and *Nostoc* sp. PCC 7120 (PDB IDs 2ZT9, 4H44, and 4OGQ) (6,25–28), and from the green alga *Chlamydomonas reinhardtii* (PDB ID 1Q90) (29). The presence of a light-harvesting pigment molecule is not expected in the structure of the cytochrome b_6f electron-proton transport complex, whose reactions are not directly light dependent. Previous studies have discussed several properties of the unique Chl molecule related to H_2O axial ligation (28), the aromatic amino acid environment (30), Chl excited-state lifetimes (31), excited-state triplet energy transfer (32), and a possible function in the regulation of photosynthetic-state transitions (33), as suggested by consideration of the evolution of the complex (34). A possible contact of the Chl phytyl chain with PQ, evident in the original crystal structures of the b_6f complex, has been noted (27,29,33). In this study, we consider the consequences of protrusion of the phytyl chain into, and partial occlusion of, the Q_p portal

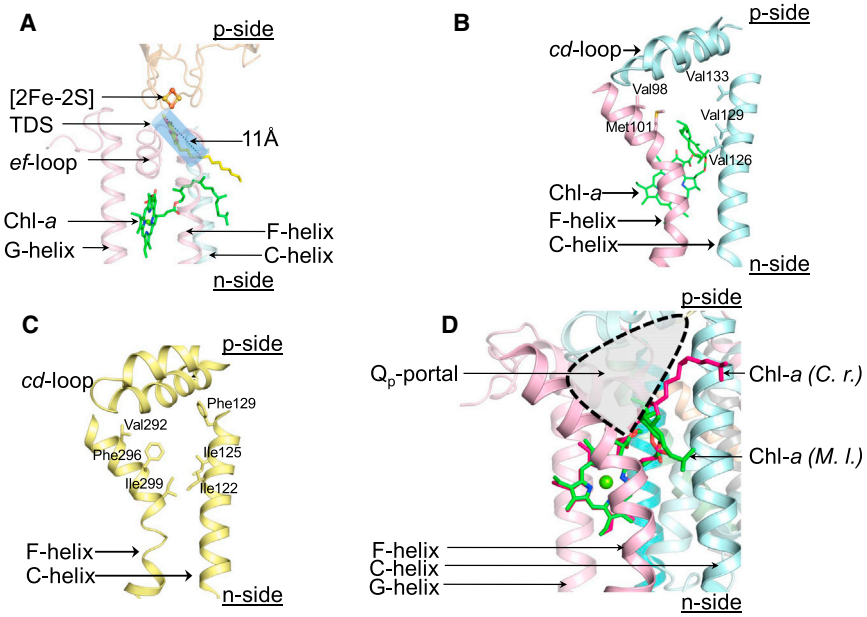

FIGURE 2 Q_p portal in cytochrome *bc* complexes. (*A*) The 11-Å-wide Q_p portal in the cytochrome b_6f complex (PDB ID 4H13). The portal is shown as a blue tunnel around the TDS molecule (*yellow/red sticks*). For reference, the *ef* loop of the cyt b_6 subunit, and the C, F, and G transmembrane helices are shown as ribbons. (*B*) Q_p portal in the cytochrome b_6f complex. C (cytochrome b_6) and F (subunit IV) transmembrane helices are shown as ribbons, and residues lining the portal are shown as sticks. The phytyl chain of the Chl molecule (*green sticks*) is inserted between the C and F transmembrane helices, thereby constricting the space available for substrate diffusion. (*C*) Q_p portal in the cytochrome bc_1 complex (PDB ID 3CX5). The C and F transmembrane helices of the cytochrome *b* subunit are shown as ribbons, and residues lining the portal are shown as sticks. (*D*) Alternate conformations of the Chl phytyl chain in the cytochrome b_6f complex. The Chl phytyl chain (*green*) is wrapped around the F helix in the cytochrome b_6f crystal structure (PDB ID 2E74) obtained from the cyanobacterium *M. laminosus* (labeled *M. l.*), whereas it occupies a niche distal to the F helix in the b_6f structure (PDB ID 1Q90) obtained from the green alga *C. reinhardtii* (*C. r.*). The Q_p portal is highlighted.

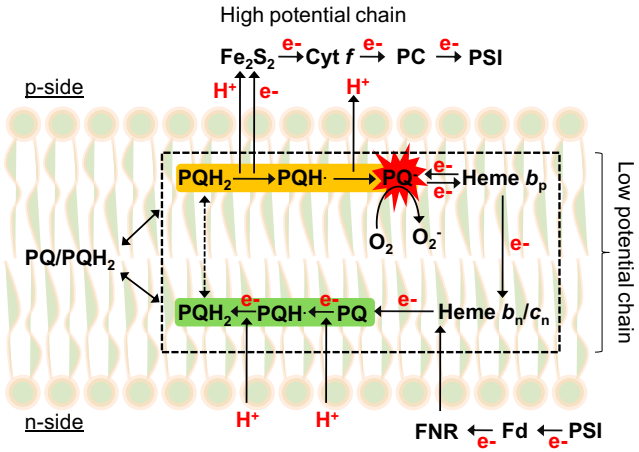

FIGURE 3 Electron-proton transfer pathways in the cytochrome b_6f complex. The dashed box represents the cytochrome b_6f transmembrane core. On the p side, anionic semiquinone ($PQ^{\bullet-}$) (highlighted in *red*) is produced by deprotonation-oxidation of the reduced plastoquinol (PQH_2), or back-transfer of an electron to the oxidized PQ from the reduced heme b_p. The anionic semiquinone has been implicated in the reduction of molecular oxygen to superoxide ($O_2^{\bullet-}$). FNR, ferredoxin-$NADP^+$-oxidoreductase; Fd, ferredoxin. To see this figure in color, go online.

(Fig. 2, *A–D*), which serves as the entrance channel for the plastoquinol electron/proton donor to the complex and the exit for oxidized deprotonated PQ. The Chl phytyl chain appears to provide a quinone/-ol traffic barrier that is absent in the cyt bc_1 complex (Fig. 2, *B* and *C*). In this regard, we note that a redox-linked conformational change in the quinol/quinone binding position within the bc_1 complex Q_p site has been implicated in the removal of the semiquinone intermediate (35).

Insights into the architecture of the Q_p portal for p-side quinol/quinone entry/exit, and the interaction of the Chl phytyl chain with this portal, have been obtained from previous crystallographic determinations of the position of the Chl molecule in the b_6f complex of cyanobacteria (6,25,27,28) and the green alga *C. reinhardtii* (29). Here, we analyzed further the spatial relation of the Chl phytyl chain and the p-side quinone portal. We report a crystal structure of the cyanobacterial cytochrome b_6f complex with the quinone analog p-side inhibitor stigmatellin, which is an effective inhibitor of the bc_1, but not the b_6f complex, and thus serves as a probe for the relative size of the Q_p portal. Results from a comparison with the Q_p portal described in a crystal structure of the yeast bc_1 complex (38), as well as a novel (to our knowledge) molecular-dynamics analysis of quinone exit from the portal, indicate that the Chl phytyl chain has a role in constraining the exit of the quinol/quinone from its charge-transfer binding site on the p side of the complex, with an implied consequence of increased quinone residence time in its p-side portal and binding site.

MATERIALS AND METHODS

Protein purification and crystallization

The purification and crystallization of the cyt b_6f complex from *M. laminosus* were described previously (28). Cocrystallization was performed with a stigmatellin/cyt b_6f monomer molar ratio of ~5:1.

X-ray diffraction data collection and data reduction

X-ray diffraction data collection was performed at 100 K using the Advanced Photon Source (Argonne IL) beamline 19-ID-B. Data reduction, including indexing, integration, and scaling, was performed in the HKL2000 suite (39). The high-resolution limit of the data set was determined according to the correlation coefficient (CC*) method described by Karplus and Diederichs (40) (Table 1). The $\langle I\rangle/\langle\sigma_I\rangle$ value, which is a measure of the average signal strength within a shell, was found to be 0.6 for the outermost shell of reflections, extending from 3.05 to 3.00 Å, with 38% completeness of the shell (Table 1; Table S1, A–C, in the Supporting Material). An analysis of the reflection intensities showed that the outermost shell was populated mainly by relatively weak reflections ($I/\langle\sigma_I\rangle < 2$) for 870 reflections (86% of outer-shell reflections; Table 1;

TABLE 1 Summary of crystallographic data

Crystal	Cyt b_6f with stigmatellin (PDB ID 4PV1)
Data collection	
Beamline	APS-19-ID
Wavelength (Å)	0.979
Space group	$P6_122$
Cell dimensions	
a, *b*, *c* (Å)	159.1, 159.1, 361.3
α, β, γ (°)	90, 90, 120
Resolution (Å)	50.00–3.00 (3.05–3.00)
CC*	0.96 (0.81)
R_{pim} (%)	3.5 (64.7)
Completeness (%)	91.4 (38.0)
Redundancy	9.8 (5.0)
Refinement	
Resolution (Å)	49.34–3.00
Reflections	50203
R_{work} (%)/R_{free} (%)[a]	21.6/24.7
Ramachandran statistics	
Favored (%)	91.8
Allowed (%)	7.8
Unfavored (%)	0.4
Rotamer outliers (%)	0.4
Number of atoms	
Protein	7330
Ligand/ion	703
Water	16
Wilson *B*-factor (Å^2)	96.6
B-factor (Å^2, average)	
Protein	115.4
Ligand/ion	109.0
Water	88.0
Root mean-square deviation	
Bond lengths (Å)	0.004
Bond angles (°)	0.646
Coordinate error (maximum likelihood, Å)	0.4

Values in parentheses correspond to the outer shell; [a]5.1% of reflections included in the R_{free} test set.

Fig. S1; Table S1, A–C). As a result, the average strength of the outer-shell signal was low, even though a significant number of strong reflections were present (146 reflections (14% of outer-shell reflections) with $<I>/<\sigma_I> \geq 2$). Based on the CC* cutoff criterion, all reflections extending up to a resolution of 3.00 Å were utilized for calculation of the electron density map.

Electron density map calculation and model building

Crystallographic data reduction showed that the unit cell dimensions had similar dimensions (space group $P6_122$, a = b = 159.1 Å, c = 361.3 Å, $\alpha = \beta = 90°$, $\gamma = 120°$) compared with the cocrystal structure of the cyt b_6f complex isolated from *M. laminosus* with bound quinone analog inhibitor tridecyl-stigmatellin (TDS; PDB ID 2E76, space group $P6_122$, a = b = 157.2 Å, c = 363.3 Å, $\alpha = \beta = 90°$, $\gamma = 120°$). The polypeptide model of the cyt b_6f complex (PDB ID 2E76) was used for rigid-body refinement in REFMAC (41). The prosthetic groups heme b_p, b_n, c_n, and *f*; [2Fe-2S] cluster; Chl; and β-Car were then built into the model in Coot (42). Restrained refinement was performed in PHENIX (43). After restrained refinement of polypeptide model with the prosthetic groups listed above, electron density was observed in the Fo-Fc and 2Fo-Fc maps at a position axial to heme c_n. A simulated annealing OMIT map was calculated around the electron density near heme c_n. A stigmatellin molecule was modeled in the electron density, with the chromone ring located proximal to heme c_n and the hydrocarbon tail pointing into the intermonomer cavity. Several cycles of manual model building and restrained refinement were performed to improve the fitting of the stigmatellin ligand in the electron density map. It is significant that no electron density was observed for stigmatellin within the Q_p site of the b_6f complex. An OMIT map (44) was calculated in PHENIX around the Q_p and Q_n sites using simulated annealing. Translation-libration-screw (TLS) refinement of atomic displacement parameters (ADPs) was performed using 26 TLS groups generated in PHENIX. The figures were generated in PyMol (http://www.pymol.org) and Coot. The model coordinates and structure factors were deposited in the PDB with ID 4PV1.

Simulation of the p-side Q_p portal of the cytochrome b_6f complex using discrete molecular dynamics

Truncated models of the structure of the b_6f complex (28) were prepared by manually removing regions distal from the Q_p portal. The truncated model of cytochrome b_6f (PDB ID 2E74) contained cytochrome b_6 (chain A, Ile-32–Leu-215), subunit IV (chain B, Gly-63–Ala-147) and the Rieske iron-sulfur protein (ISP; chain D, Pro-44–Val-92, Ala-98–Val-179). PQ-9 was manually inserted into the Q_p portal of cytochrome b_6f using the known binding configuration of TDS (PDB ID 2E76) as a guide. Simulations were performed using parallelized discrete molecular dynamics (πDMD; Molecules in Action) (45) with the Medusa force field (46), which utilizes implicit solvent. Details of the DMD algorithm have been described elsewhere (45,47,48). Briefly, DMD uses discretized energetic step functions in its force field instead of continuous potentials. A discrete representation of the force field provides advantages for the modeling of specific interactions, such as hydrogen bonding (48). The time step used to advance our simulations was 50 fs, compared with 2 fs in traditional MD. In the limit of a shortened time step, the discretized potentials of DMD would become identical to the continuous potentials of MD. The production simulation temperature was 0.4 kcal/mol-k_B (where k_B is Boltzmann's constant), with a heat exchange coefficient, which describes the exchange of energy between the system and the implicit solvent, of one. The units of time, temperature, and heat exchange in DMD have been fully described elsewhere (49). Temperature was controlled using the Berendsen thermostat (50). Chains of the protein that were not in direct contact with the quinone were held static with infinite square well constraints. Chains that had residues in direct contact with the quinone were harmonically constrained (spring-like constraints) with a spring constant of 10 kcal/mol × $Å^2$ on each atom of the protein backbone, whereas the side chains were allowed to move freely. Where present, carbon atoms 5–10 of the Chl were placed under a similar harmonic constraint to keep the Chl bound to the protein, whereas the remaining 10 carbon atoms of the phytyl tail, as well as the quinone molecule of each system, were allowed to move freely. Each system was equilibrated at high temperature (0.7 kcal/mol-k_B) and high heat exchange (10 exchanges per unit time) for 1,000 DMD time steps (~50 ps). Simulations were performed for 500,000 DMD time steps (~25 ns) to observe the behavior of the quinone and Chl phytyl tail in the portal. Production simulations were repeated in 25 replicates for each system of the structure of the b_6f complex (PDB ID 2E74) with and without the Chl molecule. The effect of the alternate Chl tail conformation on PQ retention was also investigated by utilizing the Chl conformation from the related eukaryotic b_6f structure (PDB ID 1Q90) and analyzing it in the context of the cyanobacterial b_6f structure (PDB ID 2E74).

RESULTS

Properties of the p-side quinol-binding niche

The Q_p portal provides a connection between the intermonomer cavity (Fig. 1 *B*) of cytochrome *bc* complexes, which is believed to be the site of quinone transfer to or from the quinone pool in the membrane bilayer (2,27), as well as the Q_p site of quinol deprotonation-oxidation (2), and may contribute to the heterogeneity of the dielectric constant within the complex (51). For the portals in both complexes, the substrate quinols ((plastoquinol in oxygenic photosynthesis, and ubiquinol in anoxygenic photosynthesis and mitochondrial respiration) have a long poly-prenyl chain with nine and ten prenyl units, respectively, which presumably creates a considerable enthalpic and entropic barrier for the diffusion and insertion of the substrate quinol into the narrow Q_p portal. Access to the Q_p site of cyt *bc* complexes is defined by the p-side Q_p portal that is approximately normal to the plane of the membrane (Fig. 2, *B* and *C*). The overall architecture of the Q_p portal is conserved between cytochrome *bc* complexes. The width of the portal (defined by its bordering amino acid residues) is slightly smaller in the cytochrome bc_1 complex (10–12 Å; Fig. 2 *C*), where the portal is lined by aliphatic and aromatic amino acids, than in the b_6f complex (13–14 Å; Fig. 2 *B*), where it is bordered by aliphatic residues (17). The amino acid residues that form the quinone-transfer portal belong to the C and F transmembrane helices of the cytochrome *b* subunit of bc_1, and of the cytochrome b_6 subunit and subunit IV in the b_6f complex. A sequence and structure comparison shows that the portal is lined in bc_1 by the residues Ile-122, Ile-125, and Phe-129 of the C helix, and Val-292, Phe-296, and Ile-299 of the cytochrome *b* F helix. In b_6f, the portal is defined mainly by small hydrophobic amino acids in the C-helix (Val-126, Val-129, and Val-133) and the F-helix (Val-98 and Met-101). Hence, the protein structure implies that the width of the Q_p portal should be smaller in the bc_1 complex than in the b_6f complex. However, the effective diameter of the portal in the b_6f complex is significantly reduced from the 13–14 Å defined by the amino acid

residues lining the channel due to the presence of the phytyl chain of Chl, as discussed below.

Occlusion of the quinol-transfer portal

The presence of the Chl phytyl chain that occludes the Q_p portal in the b_6f complex is a significant difference between the p-side quinol-transfer Q_p portal in the cytochrome b_6f and bc_1 complexes. The portal including the phytyl chain (28) is shown in the context of the surrounding amino acid environment in Fig. 2 *B*, and for the structures obtained from *M. laminosus* (28) and *C. reinhardtii* (29) in Fig. 2 *D*. The different positions of the Chl phytyl chain in the two structures of the b_6f complex imply either flexibility of the phytyl chain and/or more than one stable position (Fig. 2 *D*). In both structures, the presence of the phytyl chain significantly occludes the quinol-transfer portal on the p side of the complex.

Stigmatellin: a probe of the p-side portal space

To probe the accessible space of the Q_p portal within the cytochrome b_6f complex, we performed a cocrystallization study of the cytochrome b_6f complex (PDB ID 4PV1; for a summary of the crystallographic data, see Table 1) with the p-side quinone analog/inhibitor stigmatellin and compared the results with the previously reported structure of the b_6f complex with the related inhibitor TDS (PDB ID 2E76). Stigmatellin and TDS have identical cyclic chromone rings (Fig. 4, *A* and *B*) attached to a hydrocarbon tail, which is branched in stigmatellin, leading to the expectation that stigmatellin would occupy a larger volume than TDS. Stigmatellin is well known to be a substantially less effective inhibitor of electron transport in oxygenic photosynthesis compared with TDS (53), which contrasts with its well-known efficacy as a p-side inhibitor of electron transport in the bc_1 complex (54–56). It was observed that, unlike TDS (6,27–29), stigmatellin was unable to bind tightly within the Q_p portal of the b_6f complex (PDB ID 4PV1, this study).

As can be seen by a comparison of the OMIT maps for stigmatellin at the Q_n and Q_p sites, respectively (Fig. 5, *A* and *B*), although no significant electron density was observed within the Q_p site (Fig. 5 *B*), electron density was clearly defined for stigmatellin at the Q_n site (Fig. 5, *A* and *C*). At the Q_n site, the chromone ring of stigmatellin was modeled and refined proximal to heme c_n, whereas the hydrocarbon tail was mostly disordered (Fig. 5 *C*).

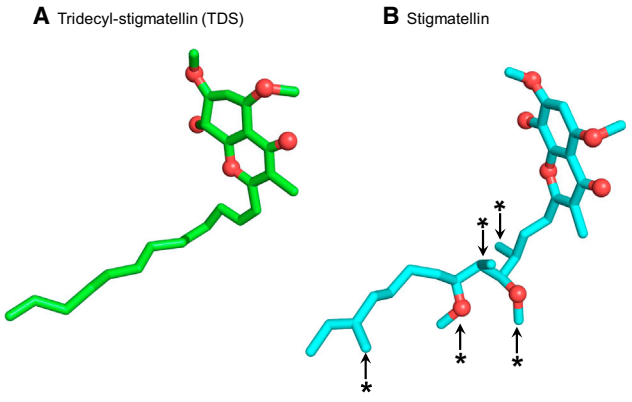

FIGURE 4 Structure of the quinone analog/inhibitors (*A*) TDS and (*B*) stigmatellin. Both inhibitors have identical chromone rings that interact with the Q_p site residues. Structural differences lie in the hydrocarbon tails of stigmatellin and TDS. The tail of TDS is unbranched, whereas that of stigmatellin is branched (branching highlighted by *arrows* and *asterisks*). The oxygen atoms are shown as red spheres. To see this figure in color, go online.

DMD simulation of quinone exit from the Q_p portal of the cytochrome b_6f complex

The effect of the presence of the Chl phytyl chain on the dynamics of the lipophilic quinone within the Q_p portal of the cytochrome b_6f complex from the cyanobacterium

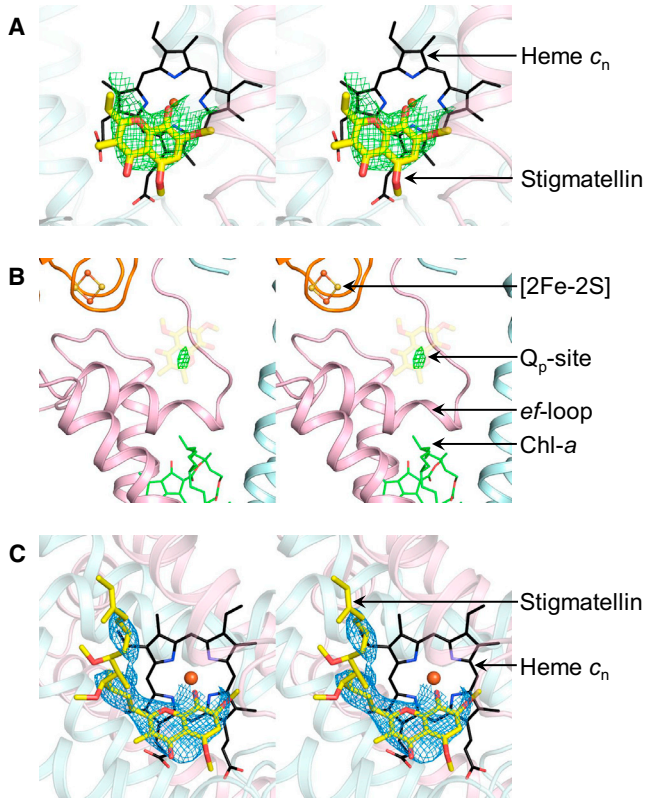

FIGURE 5 Crystal structure of the cytochrome b_6f complex with stigmatellin. (*A* and *B*) OMIT map (stereo-pair images) around stigmatellin on the (*A*) n side and (*B*) p side. Electron density is observed (*mesh, green*) on the n side in a position axial to heme c_n. However, no significant electron density feature is recorded on the p side. For clarity, only the chromone ring of stigmatellin is shown (*semitransparent*). The electron density map is contoured at 3.5 σ. (*C*) Stigmatellin bound axially to heme c_n. The 2Fo-Fc map (*mesh, blue*; contoured at 1.2 σ) shows electron density around the stigmatellin chromone ring. The distal portion of the hydrocarbon tail, located away from the chromone ring, is largely disordered. To see this figure in color, go online.

M. laminosus (PDB ID 2E74) was analyzed using DMD (45,47,48). Interactions of the PQ molecule with the amino acid residues of the Q_p portal were probed in the presence and absence of Chl. To determine whether the presence of the Chl phytyl chain affects the retention of PQ within the Q_p portal, a DMD analysis was utilized with an initial simulation on a 25 ns timescale (Table 2).

PQ was initially positioned on the p-side end of the portal proximal (2 Å) to the His-129 ligand to the [2Fe-2S] cluster of the Rieske ISP subunit. PQ translation through the Q_p portal was measured as the displacement of the C6 atom of the quinone ring (Fig. 1 *C*) from its initial position. Exit of the PQ molecule was defined as an 11 Å displacement of the C6 atom of the quinone ring (Fig. 1 *C*), equal to the length of the Q_p portal, within a time interval of 25 ns. In the presence of the Chl-phytyl chain positioned as in the cyanobacterial b_6f complex, in 25 independent repetitions of the DMD simulation, PQ exit was observed in only 13 of the 25 simulations (Table 2). In the other 12 simulations, the displacement of the PQ was <11 Å (Table 2) and was considered to be retained within the portal. The time period of PQ displacement by 11 Å was found to be 10.4 ns in the presence of the Chl phytyl tail, averaged over 13 MD trials. The simulation trials that did not result in PQ displacement by at least 11 Å from the initial position within 25 ns were not included in the calculation of the average exit time. When the alternate, extended phytyl-tail conformation was introduced from the eukaryotic *C. reinhardtii* b_6f structure (PDB ID 1Q90) into the cyanobacterial b_6f structure (PDB ID 2E74), the quinone exit time was 10.2 ns for the same 11 Å displacement (Table 2), indicating that the Chl phytyl-tail conformations observed in the cyanobacterial and algal b_6f structures have a very similar effect on PQ retention. For the 13 fastest exit times from the *C. reinhardtii* portal that correspond to the number measured for the cyanobacterial b_6f complex, the average exit time was 8.2 ns. In the absence of the Chl phytyl tail, the PQ molecule underwent a displacement by >11 Å in 22 of the 25 independent MD trials (Table 2) with an average exit time of 6.4 ns, and an average exit time of 1.9 ns for the 13 trials with shortest exit time. Hence, the PQ molecule was found to undergo exit from the Q_p portal not only faster in the absence of the Chl phytyl tail but also substantially more frequently (i.e., in 22 of 25 trials compared with 13 of 25 in the presence of the phytyl chain). It is significant to note that the Chl phytyl tail underwent extensive motion during the course of the DMD simulation (Fig. S2).

TABLE 2 Kinetics of plastoquinone exit from the Q_p portal

Run	Exit time (with *M. laminosus* Chl phytyl tail, ns)	Exit time (with *C. reinhardtii* Chl phytyl tail, ns)	Exit time (without Chl phytyl tail, ns)
1	no exit	no exit	no exit
2	no exit	no exit	no exit
3	no exit	no exit	no exit
4	no exit	no exit	21.9
5	no exit	no exit	16.9
6	no exit	no exit	15.1
7	no exit	no exit	14.3
8	no exit	no exit	10.8
9	no exit	19.5	10.1
10	no exit	16.6	9.6
11	no exit	16.6	8.9
12	no exit	14.9	8.0
13	24.4	13.1	6.2
14	23.4	12.3	4.8
15	15.4	12.0	3.7
16	14.7	11.8	3.3
17	11.2	11.1	0.2
18	10.7	10.2	2.1
19	9.9	7.7	2.0
20	8.4	6.9	0.8
21	7.3	5.9	0.7
22	3.8	4.9	0.5
23	1.9	3.7	0.4
24	1.9	3.4	0.3
25	1.5	2.8	0.2
Avg.	10.4 ± 2.1 (13)	10.2 ± 1.2 (17)	6.4 ± 1.4 (22)

The *M. laminosus* cytochrome b_6f complex structure (PDB ID 2E74) was utilized for DMD simulations to determine the effect of Chl phytyl tail on plastoquinone (PQ) retention. PQ exit is defined as displacement of the PQ ring (atom C6; Fig. 1 *C*) by 11 Å from its initial position defined proximal to the His-129 ligand of the Rieske ISP. No exit: PQ was displaced by <11 Å within the 25 ns time period of the simulation. Avg., average exit time ± standard error of mean (value in parentheses denotes trials included in calculation).

DISCUSSION

Longer residence time of quinone within the Q_p portal: steric function of the unique Chl

The proximity of the Chl phytyl chain to the Q_p portal results in a smaller cross section for quinol/quinone entry and exit via the portal in the b_6f complex compared with that in the bc_1 complex. The smaller Q_p portal in the b_6f complex (Fig. 2 *B*) compared with that of the yeast cytochrome bc_1 complex (Fig. 2 *C*) is consistent with the ability of the b_6f complex to bind TDS (28,53), which occupies a smaller volume than stigmatellin (Fig. 4, *A* and *B*) (28), within the Q_p site. The crystallographic result obtained in this study is consistent with the observation that the binding of the stigmatellin analog TDS to the b_6f complex is ~20- to 30-fold stronger than that of stigmatellin (53). The OMIT map calculated for stigmatellin shows the presence of electron density in a position axial to heme c_n (Fig. 5 *A*). A similar electron density pattern was previously observed proximal to heme c_n in the crystal structure of the cyt b_6f complex from *C. reinhardtii* (PDB ID 1Q90), obtained with TDS (29), and in an OMIT map calculated around heme c_n, in the *M. laminosus* cyt b_6f-TDS cocrystal structure (PDB ID 2E76) (28). As discussed previously (57), due to the limited availability of a selective amino acid environment, the Q_n site in the cyt b_6f complex is expected to

have a relatively lower selectivity and affinity for substrate binding than the Q_p site. These inferences about the smaller aperture of the Q_p portal caused by protrusion of the phytyl chain are illustrated by the fact that stigmatellin does not bind effectively at the b_6f Q_p site where its binding is restricted by the narrow Q_p portal, while no steric barrier prevents binding of stigmatellin on the n-side (Fig. 5, *A* and *C*).

MD analysis of portal blockage by the Chl phytyl chain

Further insight into the modification of the interactions of the substrate quinone with the cytochrome b_6f complex by the Chl molecule was derived from MD simulations that described the effect of Chl on the residence time of the substrate PQ (Table 2). A PQ exit path defined by an 11 Å displacement from the quinol charge-transfer site at the base of the Q_p portal, as shown in Fig. 2 *A*, was defined. In the presence of the phytyl chain, exit through an 11 Å displacement from the initial position at the p-side interface (Figs. 1 *D* and 2 *A*), defined statistically through 25 trials, occurred in only one-half to two-thirds of the 25 trials when the Chl phytyl tail conformation was in the position observed in cyanobacterial (28) or *C. reinhardtii* (29) b_6f structures. The average exit time of ~10 ns was recorded for PQ exit from the Q_p portal when the Chl phytyl tail was in either of the orientations observed in the cyanobacterial or *C. reinhardtii* b_6f structures (Table 2). However, in the absence of the Chl, PQ exit through the 11 Å displacement was favored in 22 of 25 trials, with an average exit time of ~6 ns for the whole set and only 1.9 ns for the set of 13 fastest trials. It is inferred that the presence of the Chl phytyl tail within the Q_p portal contributes to the retention of PQ within the Q_p site on a timescale that is short compared with the approximately millisecond step(s) associated with proton transfer from the quinol, which is the rate-limiting step in p-side electron-proton transfer (58).

The quinone that exits from the p-side portal would next encounter the intermonomer cavity domain of the dimeric complex (Fig. 1, *A* and *B*). This cavity in known to contain lipid-binding sites (7). This lipid presence in the cavity could further impede the exit of the quinone from the portal. Such an effect presumably would be common to both b_6f and bc_1 complexes.

Consequences of portal blockage by the Chl phytyl chain on the p-side reactions of the b_6f complex: enhanced superoxide production

Steric restrictions caused by Chl provide an obstruction to plastoquinol entry into the Q_p portal and thus may affect the overall rate of electron transfer through the b_6f complex. However, the isolated b_6f complex supports an electron transfer rate of ~250 electrons monomer^{-1} s^{-1} at room temperature (25,59,60), which is comparable to the activity of the isolated bc_1 complex (61). Therefore, quinol passage through the Chl-obstructed Q_p portal is not the rate-limiting step in the photosynthetic linear electron transport chain. Alternatively, it has been proposed that p-side deprotonation of the quinol molecule defines the rate-limiting millisecond step in the redox reactions of the cytochrome bc_1-catalyzed reactions (62), which would apply as well to the b_6f complex.

Superoxide generation: the alternative p-side reaction

The specific rate of superoxide generation (normalized to the electron transfer rate) is more than an order of magnitude larger in the b_6f complex than in the bc_1 complex (16). It is inferred from the data described here that this is a consequence of the increased residence time of the PQ and hence, through equilibration, of the plasto-semiquinone within the Q_p portal. This inference depends on whether electron transfer to, and reduction of, molecular oxygen in the region of the Q_p site occurs on a timescale <10 ns, which corresponds with the time boundary estimated for quinone exit from the quinone portal (Table 2). A nanosecond timescale (approximately that which is associated with electron tunneling through a electron donor-acceptor distance of 8–10 Å (63,64) and thus electron transfer from the plasto-semiquinone to heme b_p, separated by a distance of 5–10 Å (6,27–29,35)) characterizes the pathway that is responsible for energy storage in the complex. Hence, electron transfer to dissolved molecular oxygen can occur on a subnanosecond timescale (64), which is faster than the egress time of the quinone from the Q_p site. Enhanced quinone retention due to the steric effects of the Chl phytyl tail could then increase superoxide production by providing an increased lifetime of the anionic semiquinone.

Function of the enigmatic Chl in signaling

Intricate pathways have been described for ROS-mediated signaling in photosynthetic organisms in response to environmental stress (19–22). ROS generated in the chloroplast has been implicated in the regulation of nuclear genes through the activation of nuclear response pathways that are essential for homeostasis (65). Our study implies a structure-linked function of the Chl phytyl chain relevant to ROS production. As described here, the Chl phytyl chain impedes quinol/quinone dynamics within the Q_p portal of the cytochrome b_6f complex, which leads to enhanced retention of the intermediate semiquinone. Superoxide production as a structural consequence of Chl insertion into the cytochrome b_6f p-side catalytic site may thus represent an evolutionary modification crucial for stress response and a signaling system necessary for cellular homeostasis.

SUPPORTING MATERIAL

Two figures and one table are available at http://www.biophysj.org/biophysj/supplemental/S0006-3495(14)00840-6.

We thank P. Afonine, P. Plevka, V.M. Prasad, M.G. Rossmann, H. Zhang, and members of the CCP4 Workshop 2010 for helpful discussions. Diffraction measurements were facilitated by S. Ginell, J. Lanarz, and F. Rotella at Beamline-19-ID, Structural Biology Center, Advanced Photon Source, Argonne National Laboratory, operated by the University of Chicago, Argonne, LLC, for the Office of Biological and Environmental Research, Department of Energy (DE-AC02-06CH11357).

This study was supported by grants from the NIH (R01-GM038323 to W.A.C. and R01-GM080742 to N.V.D.), a Purdue University Fellowship (S.S.H.), infrastructure support from the Purdue University Center for Cancer Research (NIH P30 CA023168), and an NIH Predoctoral Fellowship from the National Institute on Aging (F31AG039266 to E.A.P.).

REFERENCES

1. Berry, E. A., M. Guergova-Kuras, …, A. R. Crofts. 2000. Structure and function of cytochrome *bc* complexes. *Annu. Rev. Biochem.* 69:1005–1075.
2. Cramer, W. A., H. Zhang, …, J. L. Smith. 2006. Transmembrane traffic in the cytochrome b_6f complex. *Annu. Rev. Biochem.* 75:769–790.
3. Crofts, A. R. 2004. The cytochrome bc1 complex: function in the context of structure. *Annu. Rev. Physiol.* 66:689–733.
4. Hasan, S. S., E. Yamashita, …, W. A. Cramer. 2011. Conservation of lipid functions in cytochrome bc complexes. *J. Mol. Biol.* 414:145–162.
5. Trumpower, B. L., and R. B. Gennis. 1994. Energy transduction by cytochrome complexes in mitochondrial and bacterial respiration: the enzymology of coupling electron transfer reactions to transmembrane proton translocation. *Annu. Rev. Biochem.* 63:675–716.
6. Hasan, S. S., E. Yamashita, …, W. A. Cramer. 2013. Quinone-dependent proton transfer pathways in the photosynthetic cytochrome b6f complex. *Proc. Natl. Acad. Sci. USA*. 110:4297–4302.
7. Hasan, S. S., and W. A. Cramer. 2014. Internal lipid architecture of the hetero-oligomeric cytochrome b6f complex. *Structure.* 22:1008–1015.
8. Cape, J. L., M. K. Bowman, and D. M. Kramer. 2006. Understanding the cytochrome *bc* complexes by what they don't do. The Q-cycle at 30. *Trends Plant Sci.* 11:46–55.
9. Cape, J. L., M. K. Bowman, and D. M. Kramer. 2007. A semiquinone intermediate generated at the Q_o site of the cytochrome bc_1 complex: importance for the Q-cycle and superoxide production. *Proc. Natl. Acad. Sci. USA*. 104:7887–7892.
10. Dröse, S., and U. Brandt. 2012. Molecular mechanisms of superoxide production by the mitochondrial respiratory chain. *Adv. Exp. Med. Biol.* 748:145–169.
11. Dröse, S., and U. Brandt. 2008. The mechanism of mitochondrial superoxide production by the cytochrome bc_1 complex. *J. Biol. Chem.* 283:21649–21654.
12. Forquer, I., R. Covian, …, D. M. Kramer. 2006. Similar transition states mediate the Q-cycle and superoxide production by the cytochrome bc_1 complex. *J. Biol. Chem.* 281:38459–38465.
13. Lanciano, P., B. Khalfaoui-Hassani, …, F. Daldal. 2013. Molecular mechanisms of superoxide production by complex III: a bacterial versus human mitochondrial comparative case study. *Biochim. Biophys. Acta.* 1827:1332–1339.
14. Muller, F., A. R. Crofts, and D. M. Kramer. 2002. Multiple Q-cycle bypass reactions at the Qo site of the cytochrome bc1 complex. *Biochemistry.* 41:7866–7874.
15. Ghelli, A., C. V. Tropeano, …, M. Rugolo. 2013. The cytochrome b p.278Y>C mutation causative of a multisystem disorder enhances superoxide production and alters supramolecular interactions of respiratory chain complexes. *Hum. Mol. Genet.* 22:2141–2151.
16. Baniulis, D., S. S. Hasan, …, W. A. Cramer. 2013. Mechanism of enhanced superoxide production in the cytochrome b(6)f complex of oxygenic photosynthesis. *Biochemistry.* 52:8975–8983.
17. Cramer, W. A., S. S. Hasan, and E. Yamashita. 2011. The Q cycle of cytochrome bc complexes: a structure perspective. *Biochim. Biophys. Acta.* 1807:788–802.
18. Sarewicz, M., A. Borek, …, A. Osyczka. 2010. Discrimination between two possible reaction sequences that create potential risk of generation of deleterious radicals by cytochrome bc_1. Implications for the mechanism of superoxide production. *Biochim. Biophys. Acta.* 1797:1820–1827.
19. Foyer, C. H., and S. Shigeoka. 2011. Understanding oxidative stress and antioxidant functions to enhance photosynthesis. *Plant Physiol.* 155:93–100.
20. Mittler, R., S. Vanderauwera, …, F. Van Breusegem. 2004. Reactive oxygen gene network of plants. *Trends Plant Sci.* 9:490–498.
21. Mittler, R., S. Vanderauwera, …, F. Van Breusegem. 2011. ROS signaling: the new wave? *Trends Plant Sci.* 16:300–309.
22. Fernández, A. P., and A. Strand. 2008. Retrograde signaling and plant stress: plastid signals initiate cellular stress responses. *Curr. Opin. Plant Biol.* 11:509–513.
23. Huang, D., R. M. Everly, …, W. A. Cramer. 1994. Characterization of the chloroplast cytochrome b6f complex as a structural and functional dimer. *Biochemistry.* 33:4401–4409.
24. Pierre, Y., C. Breyton, …, J.-L. Popot. 1997. On the presence and role of a molecule of chlorophyll a in the cytochrome b_6f complex. *J. Biol. Chem.* 272:21901–21908.
25. Baniulis, D., E. Yamashita, …, W. A. Cramer. 2009. Structure-function, stability, and chemical modification of the cyanobacterial cytochrome b_6f complex from *Nostoc* sp. PCC 7120. *J. Biol. Chem.* 284:9861–9869.
26. Yan, J., G. Kurisu, and W. A. Cramer. 2006. Intraprotein transfer of the quinone analogue inhibitor 2,5-dibromo-3-methyl-6-isopropyl-p-benzoquinone in the cytochrome b6f complex. *Proc. Natl. Acad. Sci. USA*. 103:69–74.
27. Kurisu, G., H. Zhang, …, W. A. Cramer. 2003. Structure of the cytochrome b6f complex of oxygenic photosynthesis: tuning the cavity. *Science.* 302:1009–1014.
28. Yamashita, E., H. Zhang, and W. A. Cramer. 2007. Structure of the cytochrome b6f complex: quinone analogue inhibitors as ligands of heme cn. *J. Mol. Biol.* 370:39–52.
29. Stroebel, D., Y. Choquet, …, D. Picot. 2003. An atypical haem in the cytochrome b(6)f complex. *Nature*. 426:413–418.
30. Yan, J., N. Dashdorj, …, W. A. Cramer. 2008. On the structural role of the aromatic residue environment of the chlorophyll a in the cytochrome b6f complex. *Biochemistry.* 47:3654–3661.
31. Dashdorj, N., H. Zhang, …, S. Savikhin. 2005. The single chlorophyll a molecule in the cytochrome b6f complex: unusual optical properties protect the complex against singlet oxygen. *Biophys. J.* 88:4178–4187.
32. Kim, H., N. Dashdorj, …, S. Savikhin. 2005. An anomalous distance dependence of intra-protein chlorophyll-carotenoid triplet energy transfer. *Biophys. J.* 89:28–30.
33. de Lacroix de Lavalette, A., G. Finazzi, and F. Zito. 2008. b6f-Associated chlorophyll: structural and dynamic contribution to the different cytochrome functions. *Biochemistry.* 47:5259–5265.
34. Hasan, S. S., and W. A. Cramer. 2012. Lipid functions in cytochrome *bc* complexes: an odd evolutionary transition in a membrane protein. *Philos. Trans. R. Soc. B Biol. Sci*. 367:3406–3411.
35. Crofts, A. R., B. Barquera, …, E. A. Berry. 1999. Mechanism of ubiquinol oxidation by the $bc(_1)$ complex: different domains of the quinol binding pocket and their role in the mechanism and binding of inhibitors. *Biochemistry.* 38:15807–15826.
36. Reference deleted in proof.
37. Reference deleted in proof.

38. Solmaz, S. R., and C. Hunte. 2008. Structure of complex III with bound cytochrome *c* in reduced state and definition of a minimal core interface for electron transfer. *J. Biol. Chem.* 283:17542–17549.

39. Otwinowski, Z., and W. Minor. 1997. Processing of X-ray diffraction data collected in oscillation mode. *Methods Enzymol.* 276:307–326.

40. Karplus, P. A., and K. Diederichs. 2012. Linking crystallographic model and data quality. *Science.* 336:1030–1033.

41. Murshudov, G. N., A. A. Vagin, and E. J. Dodson. 1997. Refinement of macromolecular structures by the maximum-likelihood method. *Acta Crystallogr. D Biol. Crystallogr.* 53:240–255.

42. Emsley, P., B. Lohkamp, …, K. Cowtan. 2010. Features and development of Coot. *Acta Crystallogr. D Biol. Crystallogr.* 66:486–501.

43. Adams, P. D., P. V. Afonine, …, P. H. Zwart. 2010. PHENIX: a comprehensive Python-based system for macromolecular structure solution. *Acta Crystallogr. D Biol. Crystallogr.* 66:213–221.

44. Terwilliger, T. C., R. W. Grosse-Kunstleve, …, L. W. Hung. 2008. Iterative-build OMIT maps: map improvement by iterative model building and refinement without model bias. *Acta Crystallogr. D Biol. Crystallogr.* 64:515–524.

45. Shirvanyants, D., F. Ding, …, N. V. Dokholyan. 2012. Discrete molecular dynamics: an efficient and versatile simulation method for fine protein characterization. *J. Phys. Chem. B.* 116:8375–8382.

46. Ding, F., and N. V. Dokholyan. 2006. Emergence of protein fold families through rational design. *PLOS Comput. Biol.* 2:e85.

47. Dokholyan, N. V., S. V. Buldyrev, …, E. I. Shakhnovich. 1998. Discrete molecular dynamics studies of the folding of a protein-like model. *Fold. Des.* 3:577–587.

48. Ding, F., D. Tsao, …, N. V. Dokholyan. 2008. Ab initio folding of proteins with all-atom discrete molecular dynamics. *Structure.* 16:1010–1018.

49. Ding, F., S. V. Buldyrev, and N. V. Dokholyan. 2005. Folding Trp-cage to NMR resolution native structure using a coarse-grained protein model. *Biophys. J.* 88:147–155.

50. Berendsen, H. J. C., J. P. M. Postma, …, J. R. Haak. 1984. Molecular-dynamics with coupling to an external bath. *J. Chem. Phys.* 81:3684–3690.

51. Hasan, S. S., S. D. Zakharov, …, W. A. Cramer. 2014. A map of dielectric heterogeneity in a membrane protein: the hetero-oligomeric cytochrome b6f complex. *J. Phys. Chem. B.* 118:6614–6625.

52. Reference deleted in proof.

53. Hope, A. B., and P. Valente. 1996. Inhibitor binding to isolated chloroplast cytochrome bf complex. *Photosynth. Res.* 49:37–48.

54. Iwata, S., J. W. Lee, …, B. K. Jap. 1998. Complete structure of the 11-subunit bovine mitochondrial cytochrome bc1 complex. *Science.* 281:64–71.

55. Kunze, B., T. Kemmer, …, H. Reichenbach. 1984. Stigmatellin, a new antibiotic from Stigmatella aurantiaca (Myxobacterales). I. Production, physico-chemical and biological properties. *J. Antibiot.* 37:454–461.

56. Thierbach, G., B. Kunze, H. Reichenbach, and G. Höfle. 1984. The mode of action of stigmatellin, a new inhibitor of the cytochrome b-c1 segment of the respiratory chain. *Biochim. Biophys. Acta.* 765:227–235.

57. Saif Hasan, S., E. Yamashita, and W. A. Cramer. 2013. Transmembrane signaling and assembly of the cytochrome b_6f-lipidic charge transfer complex. *Biochim. Biophys. Acta.* 1827:1295–1308.

58. Crofts, A. R., and Z. Wang. 1989. How rapid are the internal reactions of the ubiquinol:cytochrome c 2 oxidoreductase? *Photosynth. Res.* 22:69–87.

59. Zhang, H., G. Kurisu, …, W. A. Cramer. 2003. A defined protein-detergent-lipid complex for crystallization of integral membrane proteins: the cytochrome b_6f complex of oxygenic photosynthesis. *Proc. Natl. Acad. Sci. USA.* 100:5160–5163.

60. Zhang, H., J. P. Whitelegge, and W. A. Cramer. 2001. Ferredoxin:$NADP^+$ oxidoreductase is a subunit of the chloroplast cytochrome b_6f complex. *J. Biol. Chem.* 276:38159–38165.

61. Yu, L., S. Yang, …, C. A. Yu. 2009. Chapter 25 Analysis of electron transfer and superoxide generation in the cytochrome bc1 complex. *Methods Enzymol.* 456:459–473.

62. Crofts, A. R., M. Guergova-Kuras, …, S. J. Hong. 2000. Proton-coupled electron transfer at the Q(o) site: what type of mechanism can account for the high activation barrier? *Biochim. Biophys. Acta.* 1459:456–466.

63. Moser, C. C., J. L. Anderson, and P. L. Dutton. 2010. Guidelines for tunneling in enzymes. *Biochim. Biophys. Acta.* 1797:1573–1586.

64. Moser, C. C., J. M. Keske, …, P. L. Dutton. 1992. Nature of biological electron transfer. *Nature.* 355:796–802.

65. Pfannschmidt, T., K. Schütze, …, R. Oelmüller. 2001. A novel mechanism of nuclear photosynthesis gene regulation by redox signals from the chloroplast during photosystem stoichiometry adjustment. *J. Biol. Chem.* 276:36125–36130.

Traffic within the Cytochrome b_6f Lipoprotein Complex: Gating of the Quinone Portal

S. Saif Hasan,[1] Elizabeth A. Proctor,[2] Eiki Yamashita,[3] Nikolay V. Dokholyan[4] and William A. Cramer[1¶]

SUPPLEMENTARY INFORMATION

SI Table T1A. Crystallographic data summary. Average strength of reflection, i.e., $\langle I \rangle / \langle \sigma_I \rangle$, is shown as a function of resolution. CC*, the correlation coefficient for data-merging, is defined in reference (38) in the main text.

Resolution (Å)	$\langle I \rangle$	$\langle \sigma_I \rangle$	$\langle I \rangle / \langle \sigma_I \rangle$	R_{pim}	CC*	Completeness (%)
50.00-8.13	474	11.5	41.2	0.012	1	97.8
8.13-6.46	156.9	5	31.4	0.018	1	100.0
6.46-5.64	79.9	3.1	25.8	0.028	0.999	100.0
5.64-5.13	87.7	3.5	25.1	0.028	0.999	100.0
5.13-4.76	102.6	4.1	25	0.028	0.999	100.0
4.76-4.48	96.9	4	24.2	0.028	0.999	100.0
4.48-4.26	78.6	3.7	21.2	0.034	0.999	100.0
4.26-4.07	59.6	3.4	17.5	0.042	0.998	100.0
4.07-3.91	44.5	3	14.8	0.054	0.998	100.0
3.91-3.78	36.2	2.9	12.5	0.066	0.996	100.0
3.78-3.66	24.3	3	8.1	0.099	0.991	100.0
3.66-3.56	20.3	3.1	6.6	0.122	0.987	99.9
3.56-3.46	15.8	3.2	4.9	0.149	0.981	99.9
3.46-3.38	11.7	3.4	3.4	0.194	0.969	99.7
3.38-3.30	9.0	3.8	2.4	0.246	0.939	99.1
3.30-3.23	7.2	4.4	1.6	0.288	0.902	94.9
3.23-3.17	6.1	5	1.2	0.292	0.92	82.6
3.17-3.11	5.2	5.5	0.9	0.408	0.843	65.6
3.11-3.05	3.8	5.4	0.7	0.486	0.803	47.5
3.05-3.00	3.3	5.8	0.6	0.647	0.807	38.0

SI Table T1B. Crystallographic data summary. Distribution of reflections is shown as a function of resolution.

Resolution (Å)	**Total**	**(I/<σ_I>) <0**	**(I/<σ_I>) <1**	**(I/<σ_I>) <2**	**(I/<σ_I>) <3**	**(I/<σ_I>) <5**	**(I/<σ_I>) <10**	**(I/<σ_I>) <20**	**(I/<σ_I>) >20**
50.00-8.13	3018	19	38	50	68	89	149	328	2690
8.13-6.46	2872	28	60	95	131	183	340	858	2014
6.46-5.64	2823	48	107	156	207	306	567	1255	1568
5.64-5.13	2782	49	98	136	182	277	530	1239	1543
5.13-4.76	2779	44	79	131	183	286	518	1188	1591
4.76-4.48	2771	70	116	188	241	362	673	1358	1413
4.48-4.26	2748	70	123	220	298	452	837	1573	1175
4.26-4.07	2729	76	185	291	409	602	1045	1848	881
4.07-3.91	2754	106	242	376	518	785	1319	2053	701
3.91-3.78	2721	134	287	481	652	957	1505	2136	585
3.78-3.66	2729	195	410	666	878	1262	1861	2437	292
3.66-3.56	2711	218	487	772	1033	1440	2050	2523	188
3.56-3.46	2693	262	586	984	1264	1716	2269	2581	112
3.46-3.38	2723	372	796	1270	1639	2057	2465	2656	67
3.38-3.30	2677	440	966	1466	1799	2196	2526	2649	28
3.30-3.23	2567	524	1129	1654	1981	2271	2476	2549	18
3.23-3.17	2238	570	1147	1594	1840	2013	2175	2226	12
3.17-3.11	1763	470	972	1337	1522	1663	1742	1761	2
3.11-3.05	1283	375	782	1043	1144	1229	1269	1282	1
3.05-3.00	1016	342	656	870	945	987	1012	1016	0

SI Table T1C. Crystallographic data summary. Distribution of reflection strength, in percentage, is shown as a function of resolution.

Resolution (Å)	$(I/<\sigma_I>)$ <0	0≤ $(I/<\sigma_I>)$ <1	1≤ $(I/<\sigma_I>)$ <2	2≤ $(I/<\sigma_I>)$ <3	3≤ $(I/<\sigma_I>)$ <5	5≤ $(I/<\sigma_I>)$ <10	10≤ $(I/<\sigma_I>)$ <20	$(I/<\sigma_I>)$ >20
50.00-8.13	0.6	0.6	0.4	0.6	0.7	2	5.9	89.1
8.13-6.46	1.0	1.1	1.2	1.3	1.8	5.5	18.0	70.1
6.46-5.64	1.7	2.1	1.7	1.8	3.5	9.2	24.4	55.5
5.64-5.13	1.8	1.8	1.4	1.7	3.4	9.1	25.5	55.5
5.13-4.76	1.6	1.3	1.9	1.9	3.7	8.3	24.1	57.3
4.76-4.48	2.5	1.7	2.6	1.9	4.4	11.2	24.7	51.0
4.48-4.26	2.5	1.9	3.5	2.8	5.6	14	26.8	42.8
4.26-4.07	2.8	4	3.9	4.3	7.1	16.2	29.4	32.3
4.07-3.91	3.8	4.9	4.9	5.2	9.7	19.4	26.7	25.5
3.91-3.78	4.9	5.6	7.1	6.3	11.2	20.1	23.2	21.5
3.78-3.66	7.1	7.9	9.4	7.8	14.1	21.9	21.1	10.7
3.66-3.56	8.0	9.9	10.5	9.6	15.0	22.5	17.4	6.9
3.56-3.46	9.7	12	14.8	10.4	16.8	20.5	11.6	4.2
3.46-3.38	13.7	15.6	17.4	13.6	15.4	15.0	7.0	2.5
3.38-3.30	16.4	19.6	18.7	12.4	14.8	12.3	4.6	1.0
3.30-3.23	20.4	23.6	20.5	12.7	11.3	8.0	2.8	0.7
3.23-3.17	25.5	25.8	20.0	11.0	7.7	7.2	2.3	0.5
3.17-3.11	26.7	28.5	20.7	10.5	8.0	4.5	1.1	0.1
3.11-3.05	29.2	31.7	20.3	7.9	6.6	3.1	1	0.1
3.05-3.00	33.7	30.9	21.1	7.4	4.1	2.5	0.4	0.0

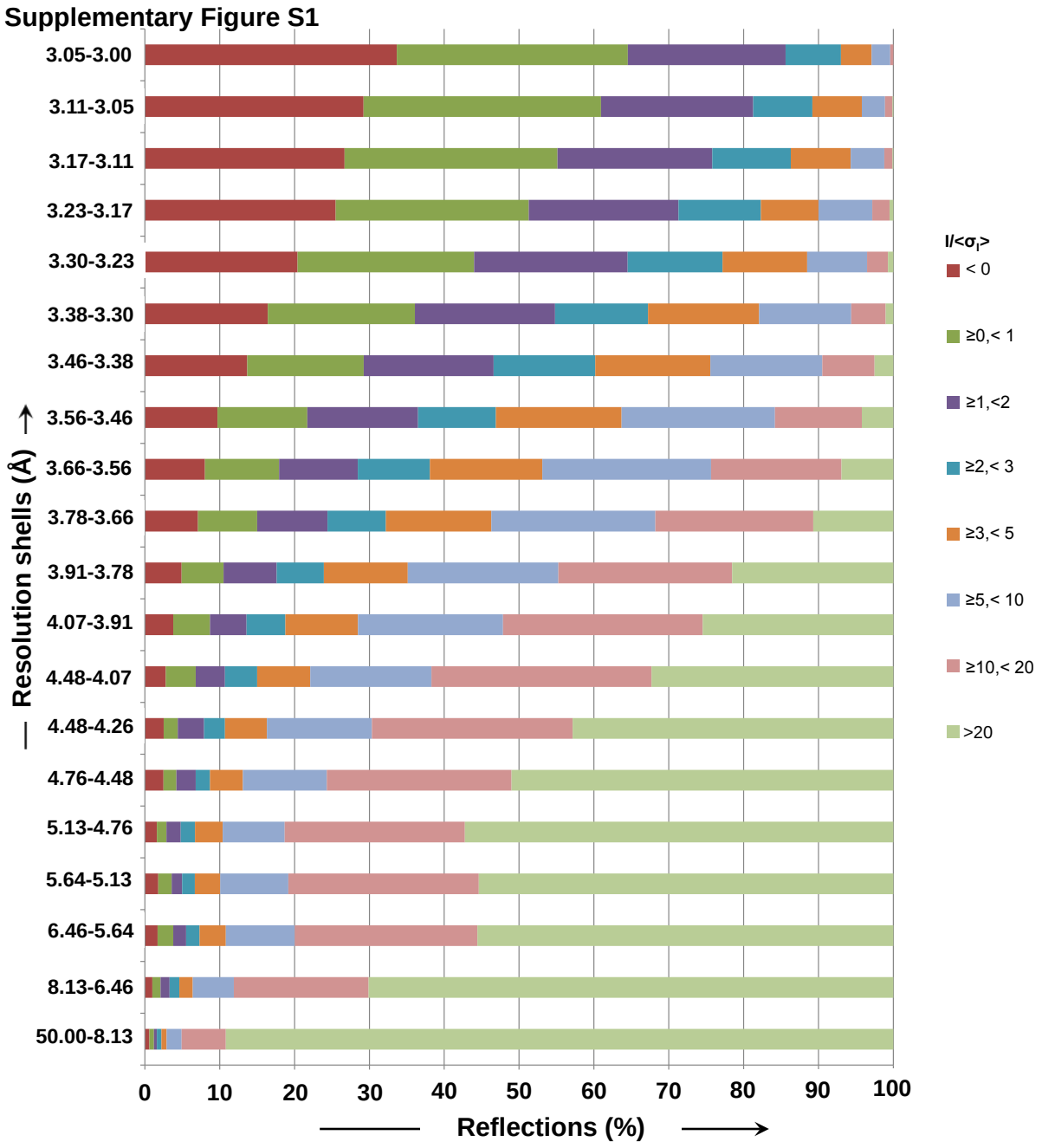

Figure S1. *Percentage of strong reflections decreases rapidly with increasing resolution.* The stronger reflections provide a measure of the average reflection strength, *i.e.*, $\langle I \rangle / \langle \sigma_I \rangle$, value per shell (see **Supplementary Table T1B,C** for details). Hence, the rapid decrease in average signal strength, *i.e.*, $\langle I \rangle / \langle \sigma_I \rangle$, is due to the decreasing contribution of the stronger reflections to the over-all average intensity. The reflection categories are color coded according to $I/\langle \sigma_I \rangle$.

Supplementary Figure S2

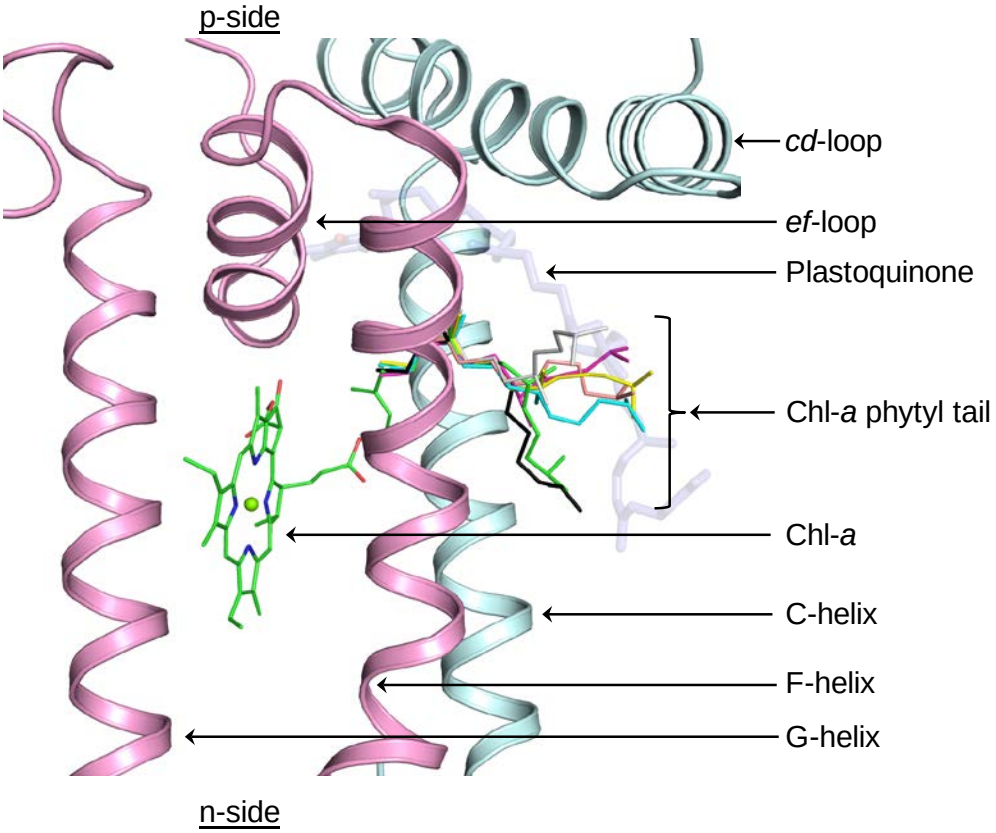

Figure S2. *Mobile phytyl-tail of Chl during DMD simulation.* The Chl phytyl-tail (shown as thin sticks) undergoes extensive motion during the course of the simulation. Color code- green, 0.0 ns; black, 2.5 ns; cyan, 5.0 ns; pink, 7.5 ns, yellow, 10.0 ns, light brown 12.5 ns; gray, 15 ns. For reference, plastoquinone bound in the Q_p-site is shown as semi-transparent thick sticks, and the protein environment is shown as ribbons (cyt b_6, cyan; subIV, pink).